PAPER

Modeling fast ion losses due to tearing and internal kink perturbations in MAST-U

IOP Publishing Plasma Physics and Controlled Fusion
Plasma Phys. Control. Fusion **67** (2025) 035016 (15pp) https://doi.org/10.1088/1361-6587/adb5b9

Modeling fast ion losses due to tearing and internal kink perturbations in MAST-U

Yueqiang Liu[1,*], J F Rivero-Rodríguez[2], S Blackmore[2], J R Harrison[2], K G McClements[2], the MAST-U Team[3] and the Tokamak Exploitation Team[4]

[1] General Atomics, PO Box 85608, San Diego, CA 92186-5608, United States of America
[2] United Kingdom Atomic Energy Authority, Culham Campus, Abingdon, Oxon OX14 3DB, United Kingdom

E-mail: liuy@fusion.gat.com

Received 5 September 2024, revised 1 February 2025
Accepted for publication 13 February 2025
Published 20 February 2025

Abstract

Fast ion (FI) loss properties in the presence of tearing mode and internal kink perturbations are numerically investigated for discharges in the MAST-U spherical tokamak, utilizing the MARS-F magnetohydrodynamic stability code and the REORBIT test particle guiding-center orbit-following module. Tracing about 100 000 particle markers sampled from the equilibrium distribution of the neutral-beam injection induced FIs, it is found that about 10% out of the total strike the limiting surface (including the divertor surface) in MAST-U discharge 46943, assuming a maximum perturbation of 100 G inside the plasma (corresponding to ∼6 G at the Mirnov probe location at the outboard mid-plane). Detailed particle tracing, assuming a uniform initial distribution in the 2D phase space (at given radial locations), reveals that initially counter-current FIs launched near the plasma edge are subject to significant prompt losses, while almost all initially co-current ions remain well confined at the assumed perturbation level. Most lost FIs strike the lower-half of the limiting surface. Finite gyro-radius effects prevent lost ions from striking the top-outer corner of the super-X divertor chamber. A scan of the perturbation level (based on discharge 45163) reveals, not surprisingly, an approximately linear scaling of the particle loss fraction (for counter-current FIs) with respect to the perturbation amplitude.

Keywords: fast ions, MHD perturbations, MAST-U

1. Introduction

It is well known that fast ions (FIs) play important roles in tokamak fusion experiments [1]. In present-day devices, most FIs come from auxiliary heating. As plasmas reach a burning state in future reactor-scale devices with deuterium–tritium fuel, the most important FI species will be fusion-born, 3.5 MeV alpha-particles. Understanding the behavior of these energetic ions in the fusion plasma, as well as their interactions with both macroscopic and microscopic perturbations inside the plasma, is of crucial importance.

With a few exceptions, present-day fusion experiments do not produce significant numbers of alpha-particles, which move faster than the Alfvén speed. Most conventional tokamak devices, with relatively large magnetic fields (typically 1–2 T), do not produce super-Alfvénic FIs through neutral beam injection (NBI), since the primary beam energy is relatively low (∼100 keV). This is however not the case in spherical tokamaks (ST) where the toroidal magnetic field is typically low (e.g. about 0.5 T in the MAST-U discharges considered in

[3] See Harrison *et al* 2024 (https://doi.org/ 10.1088/1741-4326/ad6011) for the MAST-U Team.
[4] See Joffrin *et al* 2024 (https://doi.org/10.1088/1741-4326/ad2be4) for the Tokamak Exploitation Team.
[*] Author to whom any correspondence should be addressed.

this work), and where even the NBI-induced FIs can be super-Alfvénic, making it feasible to use the present experiments to study burning plasma behaviors insofar as the energetic particles are concerned.

Another important factor is the comparable relative size of FI orbits between present-day ST devices and those of alpha-particles in a burning plasma such as ITER. Due to the compact design of STs, the ratio of the gyro-radius of the NBI-induced FIs to the plasma minor radius can reach 0.1 or even higher. The fusion-born alphas in ITER also reach this ratio of about 0.1. All these circumstances make FI studies in STs highly relevant for burning plasmas.

This work focuses on FI losses due to macroscopic magnetohydrodynamic (MHD) events in MAST-U. Deconfinement and loss of FIs due to MHD-induced three-dimensional (3D) perturbations, in particular Alfvén eigenmodes, have been well investigated [2–4]. In recent years, the role of 3D fields associated with resonant magnetic perturbations (applied to control edge-localized modes) in FI transport has also been extensively examined, both in experiments and modeling [5–7]. EP losses due to sub-Alfvén frequency MHD perturbations have also been frequently observed. Prominent examples again come from spherical tokamak devices such as MAST, where the long-lived mode (LLM) has been observed to interact with FIs and continuously impact FI confinement [8]. On the other hand, there has been little systematic modeling of FI losses due to these low-frequency MHD instabilities.

The present study aims at understanding FI losses due to low-frequency tearing mode (TM) and internal kink (IK) perturbations (the latter is responsible for certain types of LLMs) in MAST-U plasmas [9], via numerical modeling of the relevant experimental discharges. Section 2 briefly introduces the computational tools. Section 3 describes the experiment and the modeling setup, with the detailed numerical results reported in section 4. Section 5 summarizes the work.

2. Models

2.1. MHD stability model

The MHD stability analysis in this work is performed by solving the following eigenvalue problem using the MARS-F code [10] in MAST-U toroidal geometry:

$$(\gamma + in\Omega)\,\rho_1 = -\nabla\cdot(\rho\mathbf{v}), \tag{1}$$

$$(\gamma + in\Omega)\,\boldsymbol{\xi} = \mathbf{v} + (\boldsymbol{\xi}\cdot\nabla\Omega)R^2\nabla\phi, \tag{2}$$

$$\begin{aligned}\rho(\gamma + in\Omega)\,\mathbf{v} = &-\nabla p + \mathbf{j}\times\mathbf{B} + \mathbf{J}\times\mathbf{Q}\\ &+\rho\left[2\Omega\nabla Z\times\mathbf{v} - (\mathbf{v}\cdot\nabla\Omega)R^2\nabla\phi\right]\\ &+\rho_1\Omega\nabla Z\times\mathbf{V}_0,\end{aligned} \tag{3}$$

$$(\gamma + in\Omega)\,\mathbf{Q} = \nabla\times(\mathbf{v}\times\mathbf{B}) + (\mathbf{Q}\cdot\nabla\Omega)R^2\nabla\phi - \nabla\times(\eta\mathbf{j}), \tag{4}$$

$$\begin{aligned}(\gamma + in\Omega)\,p = &-\mathbf{v}\cdot\nabla P - \Gamma P\nabla\cdot\mathbf{v}\\ &+\frac{\mathbf{B}}{B}\cdot\nabla\left[\frac{\chi_{||}}{B}(\mathbf{B}\cdot\nabla p + \mathbf{Q}\cdot\nabla P)\right]\\ &+\nabla\cdot(\chi_\perp\nabla p),\end{aligned} \tag{5}$$

where γ is the (generally complex) eigenvalue and (R,Z,ϕ) are right-handed cylindrical coordinates (the equations are solved in flux-aligned curvilinear coordinates). n is the toroidal mode number ($n=1$ in this work). $\rho,\mathbf{B},\mathbf{J}=\nabla\times\mathbf{B},P,\mathbf{V}_0=R^2\Omega\nabla\phi$ are (non-dimensionalized) equilibrium quantities denoting the plasma density, magnetic field, plasma current, plasma pressure, and toroidal flow velocity (Ω is the angular frequency of the toroidal rotation), respectively. The corresponding perturbed quantities are $\rho_1,\mathbf{Q},\mathbf{j}=\nabla\times\mathbf{Q},p,\mathbf{v}$. The plasma displacement vector ξ, due to the MHD instability, is related to the perturbed velocity $\mathbf{v}$ via equation (2) in a toroidally rotating plasma. Equilibrium poloidal flows are neglected in this model.

Note two important physics effects included in the above model, which are directly relevant to the present study. One is the plasma resistivity—the last term on the right-hand side of equation (4). In this work, the resistivity coefficient η is evaluated according to the Spitzer model for the MAST-U plasma conditions (with the neoclassical corrections neglected which would typically further increases the resistivity) .

The other physics effect is associated with anisotropic thermal transport, represented by the last two terms on the right-hand side of equation (5). These two terms are derived after linearization of the full transport terms defining thermal transport parallel (with the conductivity coefficient $\chi_{||}$) and perpendicular ($\chi_\perp$) to the *total* magnetic field $\mathbf{B}+\mathbf{Q}$. Detailed derivation of these linearized terms are reported in [11]. Specifically, we point out that the term associated with $\mathbf{Q}\cdot\nabla p$ inside the brackets in equation (5) results from linearization of the parallel gradient operator taking into account the field perturbation. Note that anisotropy of the thermal transport here reflects the fact that the parallel transport is several orders of magnitude faster than the perpendicular counterpart in present-day and future tokamak devices. Thermal transport plays an important role in modifying the parallel sound wave propagation within the resistive layer, interacting with the plasma compressibility which is also included in our model [12]. Without thermal transport terms, equation (5) represents the conventional single-adiabatic closure for the MHD equations where $\Gamma=5/3$ is the ratio of specific heats.

Detailed derivations of the above equations, in the absence of the thermal transport terms, can be found from [13]. We note that these equations neglect the toroidal flow correction to the plasma equilibrium. The latter is still assumed static, which is valid if the flow speed is well below the thermal ion sound speed.

We emphasize that these equations are numerically solved in a curvilinear coordinate system (s,χ,ϕ) defined by the equilibrium magnetic flux surfaces. Fourier representations are applied along the two periodic coordinates (poloidal and toroidal angles χ and ϕ of the torus), for the solution variables $(\rho_1,\xi,\mathbf{Q},\mathbf{j},p,\mathbf{v})$. Note that χ without any subscript denotes the (generalized) poloidal angle in this work, not to be confused with the anisotropic transport coefficients mentioned earlier. A mixed-order finite element method (with staggered grids) is utilized along the radial coordinate s. As an eigenvalue solver, MARS-F employs an inverse vector iteration algorithm, where starting from a given (arbitrary) perturbation

at the first iteration, the code finds the converged eigenfunction corresponding to an eigenvalue closest to an initial guess. The code has been well tested on various MHD instabilities including the IK (e.g. in [14]) and TMs (e.g. in [12]).

2.2. FI tracing model

The test particle guiding-center orbit, in the presence of the 3D perturbations associated with the MHD instability, is traced utilizing the REORBIT module [15] originally implemented in MARS-F for relativistic electrons. In the non-relativistic limit [16], we time-advance the following equations, again in the MARS-F curvilinear coordinates

$$\frac{\mathrm{d}s}{\mathrm{d}t} = \mathbf{v}_{\mathrm{GC}} \cdot \nabla s, \tag{6}$$

$$\frac{\mathrm{d}\chi}{\mathrm{d}t} = \mathbf{v}_{\mathrm{GC}} \cdot \nabla \chi, \tag{7}$$

$$\frac{\mathrm{d}\phi}{\mathrm{d}t} = \mathbf{v}_{\mathrm{GC}} \cdot \nabla \phi, \tag{8}$$

where $\mathbf{v}_{\mathrm{GC}} = v_{\|}\hat{\mathbf{b}}_{\mathrm{tot}} + \mathbf{v}_d$, and

$$M\frac{\mathrm{d}v_{||}}{\mathrm{d}t} = Ze\left(\mathbf{E}\cdot\hat{\mathbf{b}}_{\mathrm{tot}}\right), \tag{9}$$

$$\mathbf{v}_d = \frac{1}{ZeB_{\mathrm{tot}}}\hat{\mathbf{b}}_{\mathrm{tot}} \times \left(Mv_{\|}^2\boldsymbol{\kappa} + \mu\nabla B_{\mathrm{tot}} - Ze\mathbf{E}\right) \tag{10}$$

where $\mathbf{v}_d$ is the (perpendicular) drift velocity of the particle with the charge number Z ($Z = +1$ in the present study). e is the charge unit, M the particle mass, $\kappa = (\hat{\mathbf{b}}_{\mathrm{tot}} \cdot \nabla)\hat{\mathbf{b}}_{\mathrm{tot}}$ the magnetic curvature and μ the magnetic moment. $\mathbf{E}$ is the electric field.

We emphasize that the particle guiding-center velocity $\mathbf{v}_{\mathrm{GC}}$ is calculated assuming the *total* magnetic field $\mathbf{B}_{\mathrm{tot}} = \mathbf{B} + \mathbf{Q}$. Thus in the above equations, we have $\hat{\mathbf{b}}_{\mathrm{tot}} \equiv \mathbf{B}_{\mathrm{tot}}/B_{\mathrm{tot}}$ and $B_{\mathrm{tot}} = |\mathbf{B}_{\mathrm{tot}}|$. Following the particle orbit in the curvilinear coordinates ensures high numerical accuracy, in particular when the perturbation field $\mathbf{Q}$ is also represented in the same coordinates as in our case. We note that a similar approach is followed by the VENUS-LEVIS code [17]. The difference is that VENUS-LEVIS traces FIs only inside the plasma, while REORBIT follows the particle orbit all the way to the limiting surface located in the vacuum region outside the plasma. We also note that the equilibrium flow (direct or indirect) effects on EPs are ignored in the above guiding-center model.

REORBIT considers several aspects to enable tracing particle beyond the plasma boundary. First, the self-consistently computed equilibrium field in the vacuum region is read into the module. This is important for correct description of the magnetic geometry outside the plasma including, e.g. the open-field-line regions. Next, the MARS-F computed perturbed field in the vacuum region is superposed to the equilibrium field for particle tracing. One potential issue here is the jump in the tangential components of the perturbed field across the plasma-vacuum interface, caused by the presence of the perturbed surface current at the plasma boundary. This surface current can be eliminated by carefully tailoring the equilibrium profiles to avoid finite plasma current density and pressure (and pressure gradient) at the plasma boundary. Finally, the limiting surface, which is often of odd shape as is the case in MAST-U, need to be fully enclosed by the computational domain. On the other hand, the computational mesh (in the vacuum region) should also stay within the (typically rectangular) bounding box of the equilibrium solver because the equilibrium field need to be read (and interpolated) from within the bounding box. This often requires careful generation of the computational mesh in the vacuum region outside the plasma.

3. Experiments and equilibria

3.1. Experimental observations

FI losses have been detected in MAST-U experiments due to various types of MHD activity [18]. Figure 1 shows two examples: discharges 45 163 and 46 943. The latter had a better neutral beam power capability. Here, 'SSNBI' refers to an on-axis NBI system and 'SWNBI' an off-axis system which is raised 65 cm above the vacuum vessel equatorial plane [9]. These NBI systems produce deuterium FIs with energy up to 75 keV. Multiple MHD events were detected by magnetic probes (figures 1(b) and ,(e)) during the discharges. Correlated with these events are EP losses as recorded by the FI loss detector (FILD, figures 1(c) and (f)) [19]. Note that large bursts in the FILD signal from plot (c) correspond to the fishbone-induced FI losses, which are reasonably well understood and are not studied in this work.

We will instead focus on the more continuous loss process associated with the (dominant) $n = 1$ MHD event, which we will identify as a TM coupled with a 1/1 IK component. Some of the higher-frequency branches apparent in figures 1(b) and (e) are believed to be higher-n TMs (e.g. the 3/2 component), which we do not consider in the present study. We remark that the FILD signal, while indicating the occurrence of FI losses since the instrument has not been absolutely calibrated, does not quantify the exact loss level. One purpose of the present modeling study is to make such a quantification (for a mode with a specific amplitude).

3.2. MAST-U equilibria

This work will mainly reports modeling results for MAST-U discharge 46 943. Computations have also been carried out for discharge 45 163 and we will mention some of the results in the context of discussions (only one figure will be shown concerning this discharge). The key equilibrium profiles for discharge 46 943, reconstructed at 425 ms, are plotted in figure 2. The equilibrium safety factor profile approximately settled down at the selected time slice. High-frequency perturbations also disappeared at this time as shown in figure 1(e). The vacuum toroidal magnetic field for this discharge is $B_0 = 0.52$ T at the major radius of $R_0 = 1$ m. The total plasma current is

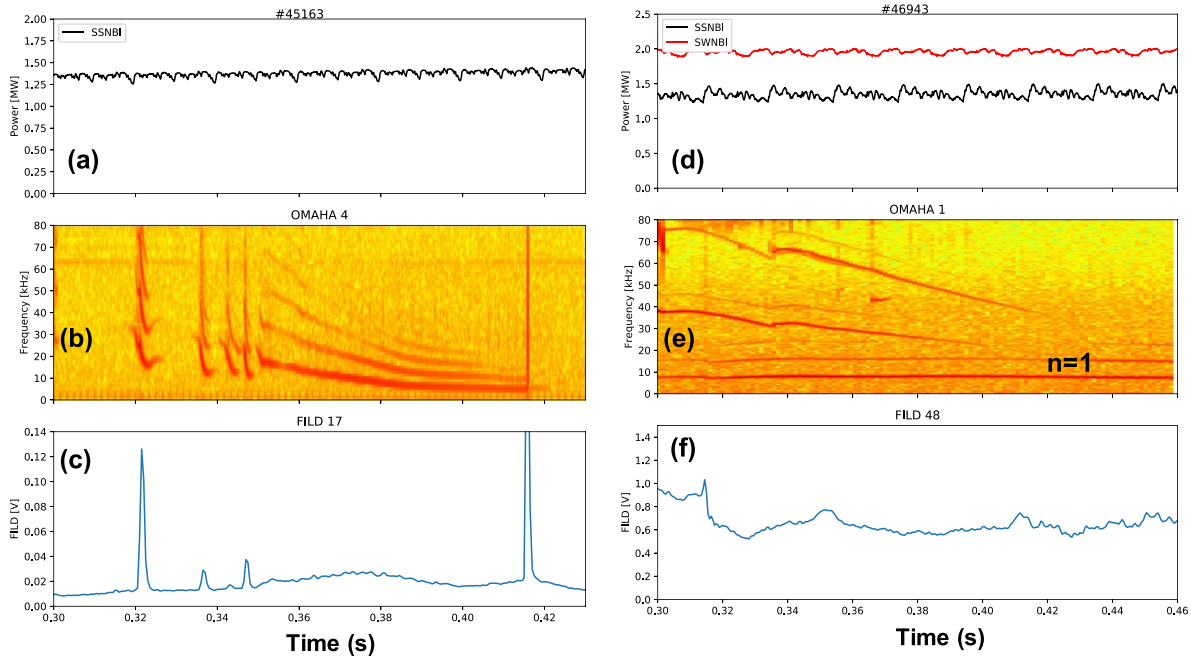

Figure 1. Experimental time traces of MAST-U discharges 45 163 (left panels) and 46 943 (right panels), for (a), (d) the neutral beam injection power, (b), (e) the frequency spectra of the magnetic perturbation measured by Mirnov coils, and (c), (f) the fast-ion loss detector (FILD) signals.

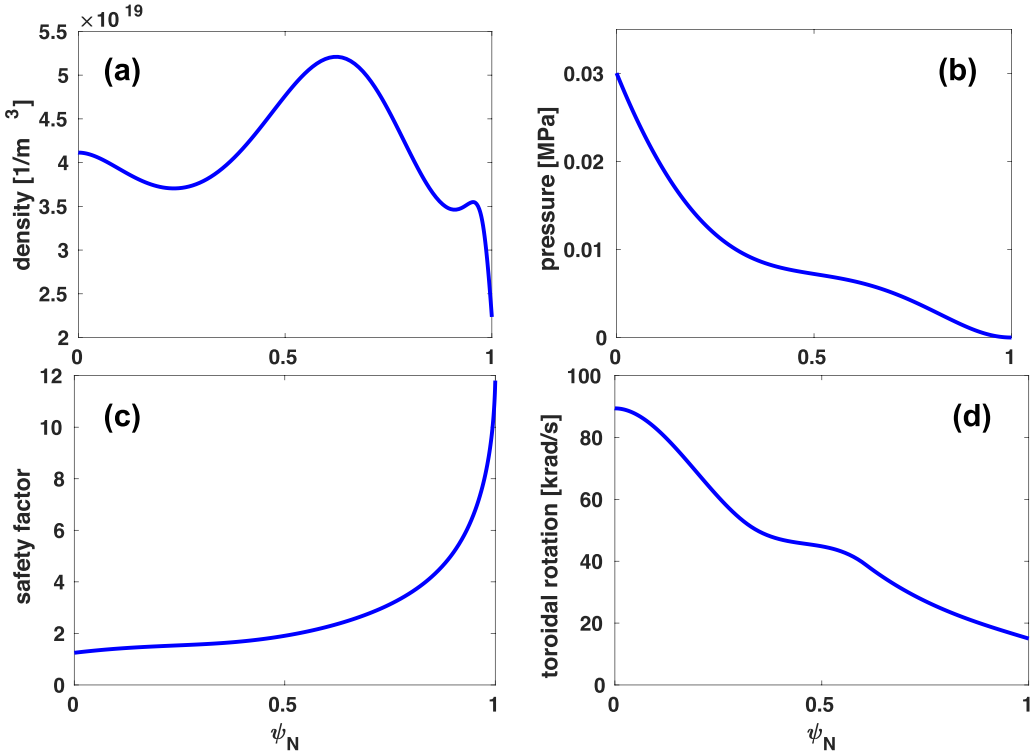

Figure 2. The equilibrium radial profiles reconstructed from MAST-U discharge 46 943 at 425 ms, for (a) the plasma density, (b) the plasma pressure, (c) the safety factor q and (d) the toroidal rotation frequency of the plasma. $\psi_N \equiv \psi_p$ here denotes the normalized equilibrium poloidal magnetic flux.

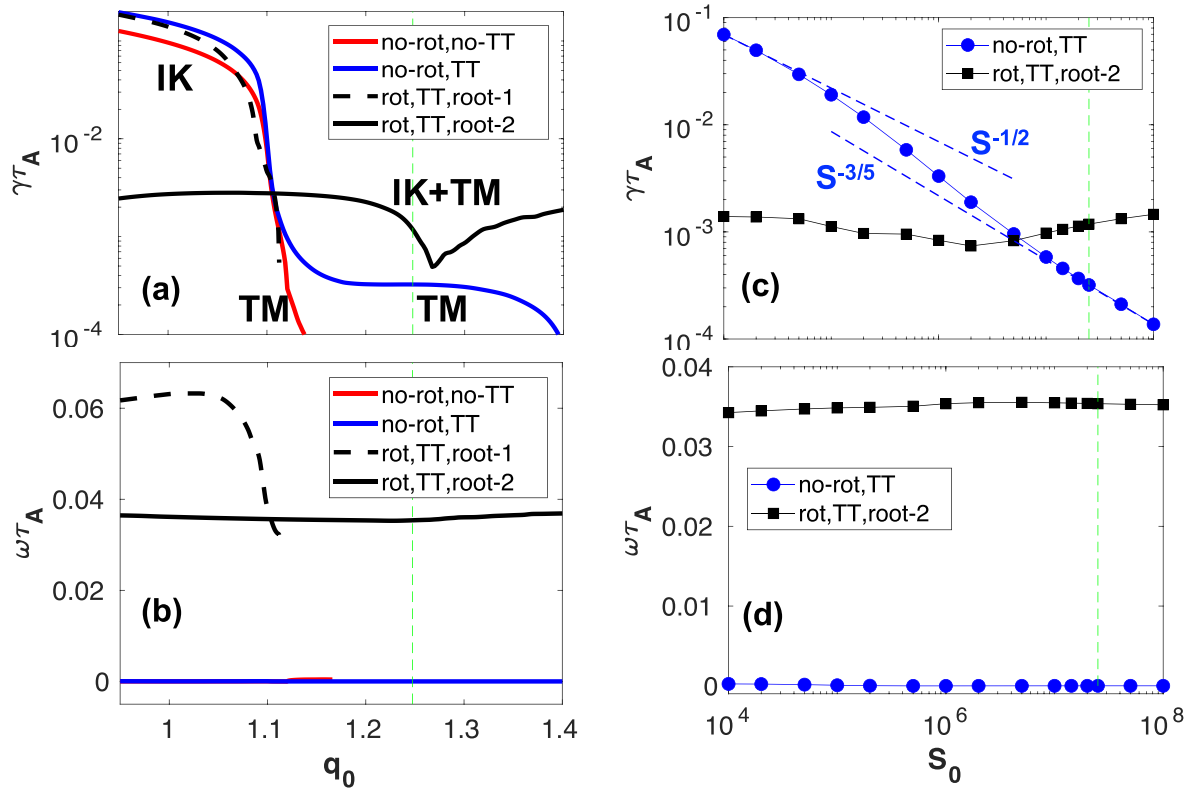

Figure 3. The (a), (c) growth rate, and (b), (d) mode frequency, of the MARS-F computed unstable MHD eigenmodes—the $n = 1$ internal kink (IK) and the $n = 1$ tearing mode (TM) - while varying (a)–(b) the on-axis safety factor q_0 (by varying the total plasma current at fixed toroidal field) at fixed on-axis Lundquist number of $S_0 = 2.5 \times 10^7$ according to the Spitzer model and (c)–(d) S_0 at fixed $q_0 = 1.248$ as in the experiment. All mode eigenvalues here are normalized by the toroidal Alfvén frequency $\omega_A = 1/\tau_A$. Various plasma conditions are assumed: vanishing plasma flow ('o-rot') and in the absence of the thermal transport ('o-TT') effect (red curves), vanishing flow but with thermal transport (blue curves), with both (experimental) plasma flow and thermal transport (black curves with solid and dashed lines indicating two branches of instability, respectively). The vertical dashed lines indicate experimental values for q_0 and S_0 from MAST-U discharge 46 943. The plasma resistivity profile follows the $T_e^{-3/2}$-scaling with T_e being the thermal electron temperature. The blue dashed lines in (c) indicate analytic scalings. Anisotropic thermal conductivity coefficients $\chi_\perp = 10^{-2}\chi_0$ and $\chi_{||} = 10^5\chi_0$ are adopted, with normalization factor $\chi_0 \equiv R_0^2/\tau_A$.

$I_p = 0.72$ MA. The normalized beta-value is $\beta_N = 2.38$. The kinetic profiles are fitted to data obtained from Thomson and charge-exchange measurements. The safety factor profile is constrained by data from the motional Stark effect diagnostic (on top of the magnetic data). Note the on-axis safety factor of $q_0 = 1.25$ which is well above unity (and even higher during the earlier time of the discharge). Nevertheless, a large 1/1 IK component still exists in the MARS-F computed unstable eigenmode structure. The plasma toroidal rotation Ω corresponds to the on-axis Alfvén Mach number (i.e. normalized by the toroidal Alfvén frequency $\omega_A = v_A/R_0$ with v_A being the Alfvén speed) of $\Omega_0/\omega_A = 7.1 \times 10^{-2}$. The toroidal rotation is included in most of the studies reported below.

4. Modeling results

This section reports the MARS-F computed MHD instabilities in MAST-U discharge 46 943 described above (see figures 1(d)–(f)), followed by the REORBIT simulation of the FI losses for the given magnetic perturbations associated with these instabilities.

4.1. TM-IK instability

We start by reporting the $n = 1$ instability scans, with results summarized in figure 3. The parameter that we scan here is the on-axis safety factor q_0 at fixed plasma resistivity and the on-axis Lundquist number S_0 at fixed q_0. Note that we elevate the whole equilibrium q-profile by varying the total plasma current (at fixed toroidal field). The radial profile of the surface-averaged toroidal current density is fixed. This allows the shape of the q-profile to remain approximately invariant (as that shown in figure 2(c)) while q_0 is scanned. As mentioned earlier, the on-axis safety factor is well above 1 for the reference equilibrium corresponding to the experimental case. A no-wall boundary condition is applied in these MARS-F computations. In other words, a large vacuum region outside the plasma is included in the modeling domain. We emphasize here that q_0 does not evolve during the MARS-F stability calculations. Linear stability eigenvalue results do not include the non-linear interaction between the perturbations and the safety factor evolution.

By scanning q_0 starting from $q_0 = 0.95$, we first identify an IK instability. The standard single-fluid, resistive MHD

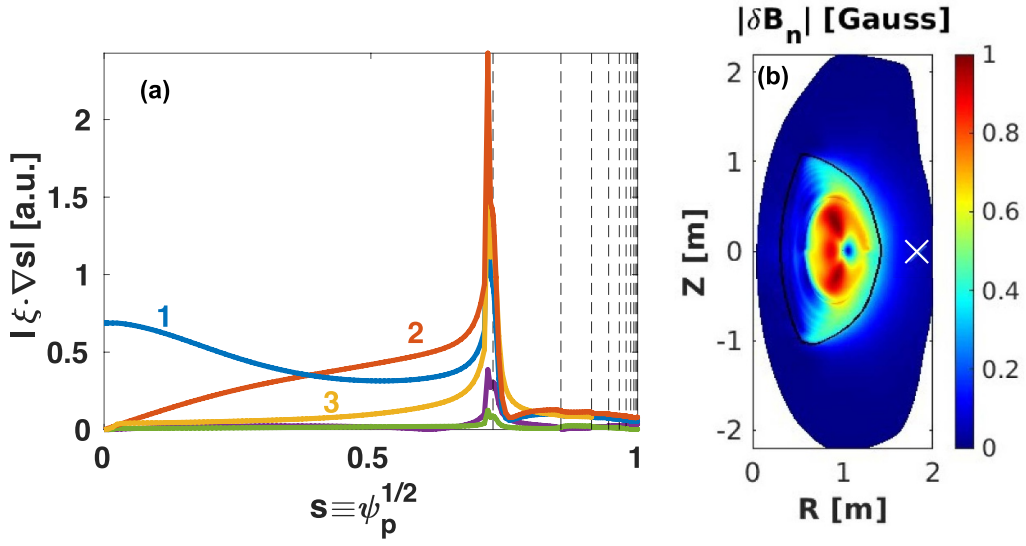

Figure 4. The MARS-F computed eigenmode structure of the $n = 1$ coupled internal kink—tearing mode, for the 'IK+TM'-branch shown in figure 3 at $q_0 = 1.248$. Plotted are (a) poloidal Fourier harmonics of the radial displacement of the plasma (in a non-straight-field-line coordinate system with the poloidal angle specified by equal arc-lengths), and (b) the magnitude of the normal component of the perturbed magnetic field inside the plasma in the poloidal plane. The labels in (a) show the poloidal harmonic numbers, with the vertical dashed lines indicating the radial location of the $n = 1$ rational surfaces (starting from $q = 2$). The '×'-sign in (b) indicates the location of one of the Mirnov probes in MAST-U and the black solid curve shows the plasma boundary.

model, without thermal transport terms and with vanishing toroidal equilibrium flow, reveals an unstable IK for $q_0 < 1.1$ (the solid red curve in figure 3(a)). With further increase of q_0, this IK is replaced by a TM which remains unstable for $q_0 < 1.13$. Note that the type of the instability is identified here by the computed eigenmode structure, with one example shown later. With the above assumptions, no instability is found for q_0 exceeding 1.13.

Adding the anisotropic thermal transport effect (blue curves in figure 3) slightly destabilizes the IK mode (at $q_0 < 1.1$). More importantly, the q_0-domain for the unstable TM is significantly extended (up to $q_0 \sim eq 1.4$) in this MAST-U plasma (figure 3(a)). This is a well-known effect of TM destabilization by anisotropic thermal transport [20], with the latter essentially playing a role of negating the stabilizing effect associated with the favorable average curvature in toroidal magnetic geometry [21].

Indeed, by artificially scanning the plasma resistivity, we find that the mode growth rate scales well as $S_0^{-3/5}$ at large values of S_0 and in the absence of the plasma flow (the blue curve in figure 3(c)), indicating a TM-dominant regime with the favorable curvature stabilization mitigated by thermal transport. At too large plasma resistivity (i.e. small S_0-values), the mode becomes a strongly unstable global resistive kink encompassing both the IK and TM characteristics, where the $S_0^{-3/5}$-like TM-scaling fails. We added an analytic curve of $S_0^{-1/2}$ in figure 3(c) to guide the eye for this high-resistivity limit. We remark that the numerical data here does not follow other analytic scalings (e.g. $\gamma \sim S^{-3/8}$ or $\gamma \sim S^{-3/13}$) found for an infernal mode coupled to a sideband tearing harmonic [22] - the dominant instability is still the TM (at large S-values) in our case.

With further inclusion of the (experimental) toroidal flow of the plasma, MARS-F reveals two branches of instability. One branch ('root-1' indicated by black dashed curves in figure 3(a)) corresponds to the IK which rotates roughly with the plasma near the axis (not near the $q = 2$ surface). This branch is however fully stabilized by the plasma flow when q_0 exceeds 1.1 (i.e. no residual TM instability occurs here). The other branch ('root-2' indicated by black solid curves in figures 3(a) and (c)) is robustly unstable across all q_0 and S_0 values. This branch contains both IK and TM components at the experimental value of the plasma resistivity (figure 4). It is also interesting that the mode growth rate varies weakly with the assumed plasma resistivity (black curve in figure 3(c))- the stability of the mode is primarily dictated by the plasma flow (and flow shear). Because of the robustness of the instability, we hypothesize that this second branch (root-2) is responsible for the observed $n = 1$ MHD activity in experiments (figure 1(e)).

Furthermore, the computed mode frequency for this branch, $\omega\tau_A = 3.54 \times 10^{-2}$ for the reference equilibrium (at $q_0 = 1.248$ and $S_0 = 2.5 \times 10^7$), corresponds to about 7 kHz which agrees well with that of the observed $n = 1$ perturbation frequency in the MAST-U discharge as documented in figure 1(e). Note that this mode frequency, roughly corresponding to the plasma rotation frequency at the $q = 2$ surface, is insensitive to the variation in the equilibrium safety factor (as is the case also in the experiment) and in the plasma resistivity. Although thermal transport plays an important role in establishing the instability as observed in the experiment,

we remark that this effect is not relevant to the EP tracing reported later on. Although not shown here, we have also computed the MHD instability for discharge 45 163. MARS-F indicates that only the IK mode is unstable in this discharge.

Figure 4(a) shows the eigenfunction of the second branch from figure 3 for the reference equilibrium from discharge 46 943, including both the toroidal rotation and the anisotropic thermal transport effect. The eigenfunction is represented by the poloidal Fourier harmonics of the radial displacement of the plasma associated with the instability. It is evident that the eigenfunction contains both a large 1/1 IK component in the plasma core and the 2/1 tearing component near the $q=2$ surface. Note that only the dominant poloidal harmonics are plotted in figure 4(a)—the MARS-F computation included 50 poloidal harmonics in total to ensure numerical convergence.

The corresponding magnetic perturbation, in terms of the perturbed normal magnetic field δB_n, is shown in figure 4(b) in the poloidal plane covering both the plasma and vacuum regions (enclosing the limiting surface as well). Note the large, internal-kink-like perturbation in the middle of the plasma column. Outside this region, the magnetic perturbation is small at the high-field side of the torus but reasonably large at the low-field side. Note also that we normalize the peak amplitude of δB_n to 1 G in this plot. Of course the overall magnitude of a linear eigenfunction has no physics significance. On the other hand, for the EP loss modeling, it is important to know the perturbation amplitude. The eigenvalue calculation obviously cannot produce such information. In this study, we therefore have to assume a certain overall amplitude for the perturbation, while using the eigenfunction to describe the detailed perturbation structure over space.

We find that, by assuming a peak perturbation of $\max|\delta B_n| = 100$ G inside the plasma, the corresponding value at the outboard mid-plane Mirnov probe location (indicated by a '×'-symbol in figure 4(b)) in MAST-U is 5.86 G, which should be in the right range compared to the experiment. (It should be noted that calibrated Mirnov data are not yet available in MAST-U experiments.) The assumed perturbation amplitude corresponds to the $n=1$ island size of about 7 cm at the $q=2$ surface. On the other hand, the 2/1 island size inferred from the Thomson scattering data (based on the local flattening of the measured electron temperature profile) reaches about 6 cm at the $q=2$ surface. This shows that the assumed perturbation level is not far from (but likely exceeds) that occurring in the experiment. Given the uncertainties associated with the linear approximation for estimating the island size in the modeling (as opposed to the non-linear islands as measured in experiment) among other factors, we do not seek exact match of the perturbation levels. In what follows, we will therefore mainly assume the peak perturbation of $\max|\delta B_n| = 100$ G inside the plasma, due to the TM-IK instability, when we trace the FI orbits. Note that a 100 G perturbation inside the plasma corresponds to about 2% of the equilibrium toroidal field (∼20% of the poloidal field) for the MAST-U plasma considered. A perturbation larger than this would significantly impact the plasma equilibrium. A scan of the perturbation amplitude $\max|\delta B_n|$ was also carried out.

We provide one more remark on the above scaling procedure in particular with respect to the magnetic island size. Although linear MHD model is only valid within the small island approximation, we can still obtain large islands by scaling the MARS-F computed eigenfunction. This is because the island size scales as the square root of the amplitude of the perturbed resonant radial magnetic field (at the corresponding mode rational surface). Indeed, by imposing the scaled perturbation onto the equilibrium field and performing field line tracing, large magnetic islands will show up on the Poincaré plot even using the linear eigenfunction. We caution that such large islands would not be identical to the nonlinear island though, partly because a linear model cannot include multiple toroidal harmonics thus cannot simulate, e.g. local flattening of the electron temperature due to large islands.

4.2. FI losses with parametric scans

We start the FI loss modeling by assuming simple particle distributions with certain parametric scans. Results obtained with this approach are useful in understanding detailed particle loss properties. These results will then be complemented by large-scale orbit-following simulations assuming realistic equilibrium distributions of FIs in MAST-U in multi-dimensional space, to be reported in section 4.3. In what follows, we will mostly neglect FI collisions and electric field acceleration. The particle energy and magnetic moment (to the lowest order) are therefore conserved during the guiding-center orbit tracing. The effect of the electric field on EP losses is addressed in the final simulation reported in the last figure of the paper.

Figures 5–7 show the REORBIT guiding-center tracing results for discharge 46 943, where we launch 1800 FIs from a uniformly-populated 2D-space of the particle (kinetic) energy ε and pitch $\lambda_0 \equiv (v_\perp^2 B_0)/(v^2 B_{\rm tot})$. Here, $v_\perp$ and v refer to the perpendicular (to the total magnetic field including both the equilibrium field and the perturbed field due to the unstable $n=1$ TM-IK) and the total guiding-center velocities of the particle, respectively. $B_{\rm tot}$ is the total field magnitude as mentioned earlier. We also launch FIs from several radial locations, corresponding to $\psi_p = 0.1, 0.3, 0.6$ and 0.9, with different REORBIT runs. All particles are launched from the outboard mid-plane and in the presence of the perturbation field with $\max|\delta B_n| = 100$ G inside the plasma (as stated earlier).

It is evident from figure 5 that (i) all initially co-current particles (with $\sigma = +1$) remain confined after 16 ms of the orbit tracing. This is the maximum tracing time imposed in these simulations, which also ensures saturation of the particle loss fraction to be shown later. (ii) Only initially counter-current FIs launched near the edge of the plasma ($\psi_p = 0.6$ and 0.9 in our cases) are subject to significant losses. As will be shown later, most of these losses are the first orbit losses which occur even without the MHD perturbations.

The final locations of all particles in the poloidal plane are shown in figure 6. Note again that in each panel, particles are

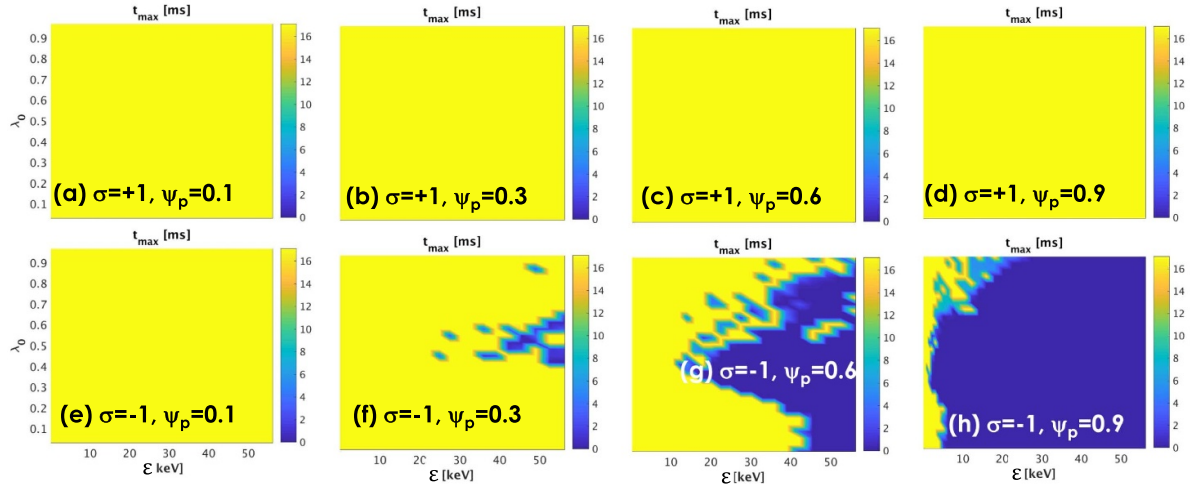

Figure 5. Loss pattern of FIs in the initially uniform launch space of the particle energy and pitch $\lambda_0 \equiv (v_\perp^2 B_0)/(v^2 B_{\rm tot})$, for both co- ($\sigma = +1$, upper panels) and counter- ($\sigma = -1$, lower panels) current ions launched from the radial location of (a), (e) $\psi_p = 0.1$, (b), (f) $\psi_p = 0.3$, (c), (g) $\psi_p = 0.6$ and (d), (h) $\psi_p = 0.9$. All particles are launched from the outboard mid-plane. The color in the plots indicates the simulation time (in ms) for lost particles prior striking the limiting surface, or the total simulation time for confined particles. The $n = 1$ magnetic perturbation inside the plasma is assumed to be 100 G for the peak value of the normal field component, corresponding to 5.86 G at the Mirnov probe location shown in figure 4(b).

initially launched from a single location (at the outboard mid-plane of a given magnetic flux surface). For the initially co-current FIs (upper panels of figure 6), although the particle orbits diffuse away from the initial surface, confinement of these particles (inside the plasma) is evident. The initially counter-current ions are subject to (mostly prompt) losses (lower panels of figure 6) when they strike the limiting surface of MAST-U. Note the specific strike points for the cases of the launching locations $\psi_p = 0.6$ and 0.9. In particular, we find a non-uniform distribution of lost FIs along the limiting surface. These strike patterns will be largely confirmed with much finer simulations to be reported in section 4.3.

The fact that the simulated orbit losses occur only for particles launched towards the plasma edge, as shown in figures 5 and 6, indicates that the $m/n = 1/1$ IK perturbation has little effect on the EP loss in MAST-U. Most of the losses are due to perturbations associated with the TM.

Figure 7 shows more loss properties of the counter-current ions, which are of our primary concern because the co-current FIs remain confined. With the final locations of all FIs, launched from different radial coordinates, being plotted together (figure 7(a)), we can divide these particles into three groups: (i) those confined within the plasma, (ii) those staying outside the plasma but not striking the limiting surface (at least after the imposed maximum tracing time), and (iii) those that strike the limiting surface (often after a short tracing time). Only particles from group (iii) are defined as lost.

Fractions of lost ions over the total number of initially launched particles are plotted in figure 7(b) versus the simulation time for different launching radii. With the perturbation level assumed here, we find that about 70% of counter-current FIs located near the plasma edge ($\psi_p = 0.9$) are eventually lost to the limiting surface. It is important to note that the majority of these losses are due to the un-confined orbits in the equilibrium magnetic fields, i.e. the so-called prompt losses that occur well within 1 ms after the particles are launched.

Similar modeling has also been performed for MAST-U discharge 45 163, where only the $n = 1$ IK is computed to be unstable using MARS-F for the target equilibrium. The overall EP loss properties are found to be similar to those reported above for discharge 46 943. Following the same method of launching FIs and assuming the same peak perturbation of 100 G inside the plasma, we find using REORBIT somewhat higher loss fraction for counter-current particles ($\sim$90% for particles launched at $\psi_p = 0.9$ and $\sim$60% for particles launched at $\psi_p = 0.6$), than that for discharge 46 943. Less than 4% loss is also simulated for the initially co-current particles in this discharge. Most of the lost FIs strike the lower portion of the limiting surface, as in figure 6. We note that the toroidal field in MAST-U is oriented such that the ion ∇B and curvature drift direction is downward rather than upward.

Further sensitivity studies have been carried out for discharge 45 163. For instance, we have also uniformly launched FIs in a 2D space of the radial coordinate ψ_p and the particle energy ε, while fixing the particle pitch (at $\lambda_0 = 0.9$, i.e. mostly trapped particles) and the overall perturbation amplitude (at 100 G). In this case, higher loss fractions are generally predicted ($\sim$ 5% for co-current FIs and $\sim$66% for counter-current FIs) than those obtained with the uniform launching of FIs in the particle phase space.

With the same setting (i.e. fixing $\lambda_0 = 0.9$), we have also scanned the overall perturbation amplitude for discharge 45 163. The results generally show, not surprisingly, that a higher perturbation level yields a larger fraction of particle losses (figure 8), for both co- and counter-current ions. In particular, the loss fraction scales approximately linearly with

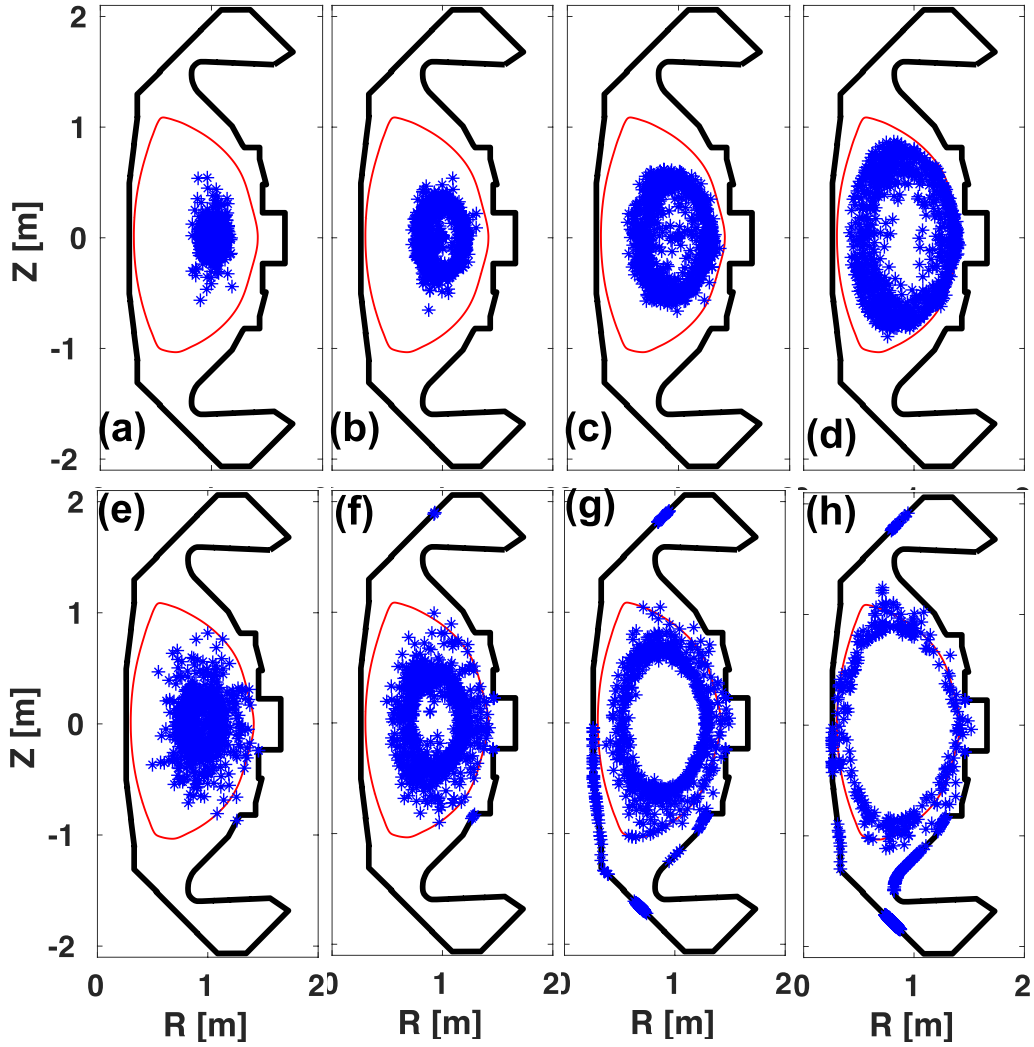

Figure 6. The final locations of the ensembles of FIs whose orbits were used to generate figure 5, in the poloidal plane. The panel labels (a)–(h) also correspond to those in figure 5. The thin red lines indicate the plasma boundary and the thick black lines the MAST-U limiting surface.

the perturbation amplitude for counter-current FIs. Perhaps a slightly surprising observation is the non-monotonic behavior of the loss fraction for the co-current ions, near $\delta B_{\max} = 800$ G. Careful examination of individual particle orbits indeed confirms that this is possible, i.e. there are particles launched with exactly the same initial conditions, but remain confined inside the plasma at $\delta B_{\max} = 1000$ G but are lost to the limiting surface at $\delta B_{\max} = 800$ G. We emphasize, however, that this non-monotonic behavior is unlikely to occur in the experiment, since a perturbation of a few hundreds G (inside the plasma) unlikely happens before the plasma equilibrium is destroyed.

4.3. FI losses with equilibrium distribution

In order to produce more quantitative understanding of the MHD-induced FI losses in MAST-U, we also perform REORBIT tracing for a much larger number of particles and for a (relatively) long time. We initiate about 100 000 particle markers sampled from the equilibrium distribution of FIs in the 4D space $(R, Z, \varepsilon, v_{||}/v)$ calculated using the ASCOT code [23]. This equilibrium distribution was obtained after reaching full (slowing-down) relaxation of EPs in the equilibrium field. This distribution is thus toroidally symmetric.

The initial distribution of the FIs produced by NBI in MAST-U discharge 46 943 is shown in figure 9(a) in the particle energy and pitch space. Shown in color here is the number fraction of FIs (over the total number of particles). Most ions are co-passing and have energy below 40 keV. Figure 9(b) shows the normalized (to unity for the peak value) particle distribution in the configuration space. It is evident that FIs are initially well-confined in the plasma core. The initial locations of the particle markers are also plotted in figure 9(c) in the 2D space of $(P_\phi, \mu B_0/\varepsilon)$. This initial marker distribution will be compared with the final ones in the presence of the $n = 1$ TM-IK, to be reported later. The peak perturbation amplitude (inside the plasma) due to the TM-IK was

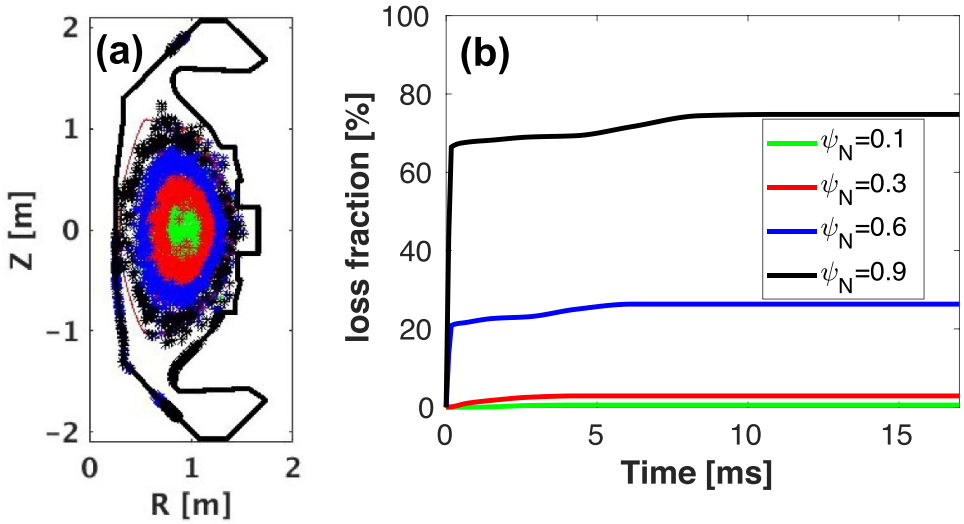

Figure 7. Further detail on the losses of counter-current FIs reported in the lower panels of figure 5: (a) the final location of all particles launched from various minor radii (indicated by different colors) and (b) the lost particle fraction versus the tracing time. The thin red lines in (a) indicate the plasma boundary and the thick black lines the MAST-U limiting surface.

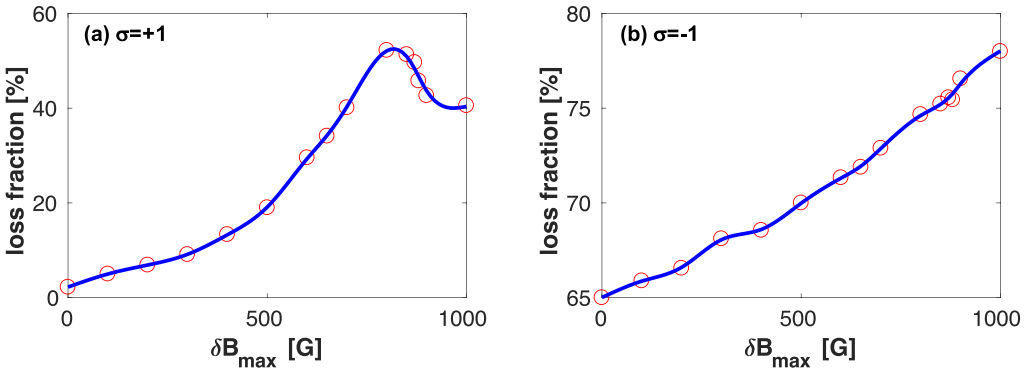

Figure 8. The simulated (final) FI loss fraction versus the assumed IK perturbation amplitude—the peak value of the $n = 1$ magnetic field inside the plasma—for MAST-U discharge 45 163 and for either (a) co-current or (b) counter-current particles. The FIs are launched with a uniform distribution in the 2D space of the radial coordinate and particle energy, and with a unique particle pitch of $\lambda_0 = 0.9$.

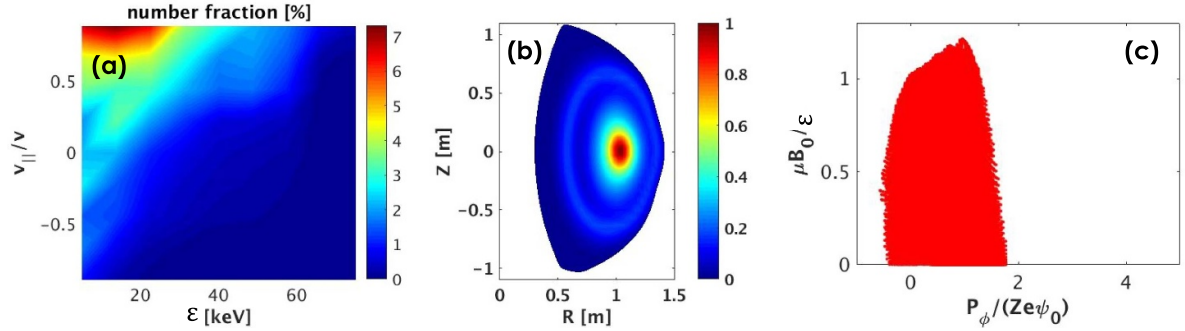

Figure 9. The ASCOT-simulated equilibrium distribution of FIs in MAST-U discharge 46 943, in (a) the particle phase space of energy ε and velocity pitch $v_{||}/v$ and (b) the configuration space (R, Z). (c) The launch positions of particle markers in the 2D space of the normalized canonical toroidal angular momentum P_ϕ and $\mu B_0/\varepsilon = \lambda_0$ with μ being the magnetic moment of the particle.

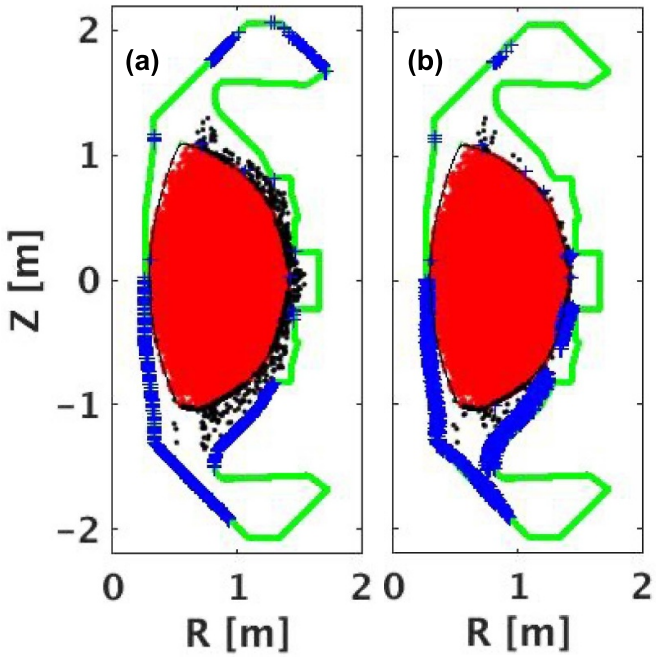

Figure 10. The final locations of all particle markers in the poloidal plane, with the maximum tracing time of $30\,000\tau_A$ (23.8 ms). All markers are launched from inside the plasma according to the equilibrium distribution, and classified in three groups according to the final location: those confined inside the plasma (red dots), those confined in the vacuum region outside the plasma after the maximum tracing time (black dots) and those lost to the limiting surface (blue '+'). The thin black line indicates the plasma boundary and the thick green line the MAST-U limiting surface. Shown here are two simulations following (a) the FI guiding-center all the way to the limiting surface, and (b) the FI guiding-center inside the plasma but taking into account the full orbit (i.e. finite gyro-radius) effect as the particle approaches the limiting surface. The overall magnitude of the $n = 1$ TM+IK perturbation inside the plasma is assumed to be 100 G (for the peak value of the normal magnetic field component), corresponding to 5.86 G at the Mirnov probe location shown in figure 4(b).

again assumed 100 G. Note that P_ϕ here denotes the canonical toroidal angular momentum of the particle and μ the magnetic moment

$$P_\phi = Ze\psi_p - MR^2\dot{\phi}, \qquad \mu = \frac{Mv_\perp^2}{2B_{\rm tot}}, \tag{11}$$

where $Z = 1$ and M is the particle mass. $\dot{\phi}$ is the particle guiding-center angular velocity in the toroidal direction (see equation (8)).

The final locations of all the particle markers due to 3D perturbations, after a maximum simulation time of $30\,000\tau_A$ (about 23.8 ms), are plotted in figure 10 in the poloidal plane. [As will be shown later, the chosen time period ensures saturation of the particle loss fraction.] Two types of orbit tracing are performed for comparison. Shown in figure 10(a) is the guiding-center ('GC') orbit-following all the way to the limiting surface—particles are considered lost when their guiding-center orbits intersect the limiting surface.

Shown in figure 10(b) is a slightly improved tracing, by taking into account the finite gyro-radius effect of high-energy ions. More specifically, as the particle approaches the limiting surface, we also add, ad hoc, the gyro-motion on top of the guiding-center motion (appendix). This approach, which we refer to as full-orbit ('FO') although it does not take into account errors arising from the neglect of finite Larmor radius effects in the orbits of particles before they approach the limiting surface, allows certain particles to intersect the limiting surface (and thus be lost) before the guiding-centers do so. This can be viewed as an approximate way of taking into account the full orbit effect, insofar as the FI loss is concerned.

We point out that this ad hoc 'FO'-tracing is useful, since in tight aspect-ratio devices such as MAST-U, deeply trapped FIs have large gyro-orbits compared to the device size. For instance, a FI with 10 (50) keV perpendicular energy has a gyro-radius of $0.085a$ ($0.19a$) where a is the plasma minor radius, assuming $B_0 = 0.52$ T (as for discharge 46 943).

We also comment here on the validity of the lowest order guiding-center approximation for EP tracing in ST plasmas, in view of the large Larmor radius compared to the plasma minor radius as mentioned above. A more rigorous simulation certainly requires inclusion of higher-order correction terms, or even the full-orbit tracing of the whole trajectory of the particle (i.e. not in the ad hoc sense mentioned above). We point out, however, several justifications for the guiding-center approach adopted in this study. The first is the time scale. As shown in figure 7(and to be further confirmed later), most orbits are either promptly lost or lost within a small number of toroidal periods of the perturbation. The higher-order correction to the guiding-center orbits should thus play a limited role within this short time. Even at longer time scale with the 3D perturbation produced by resonant magnetic perturbation in a MAST-like

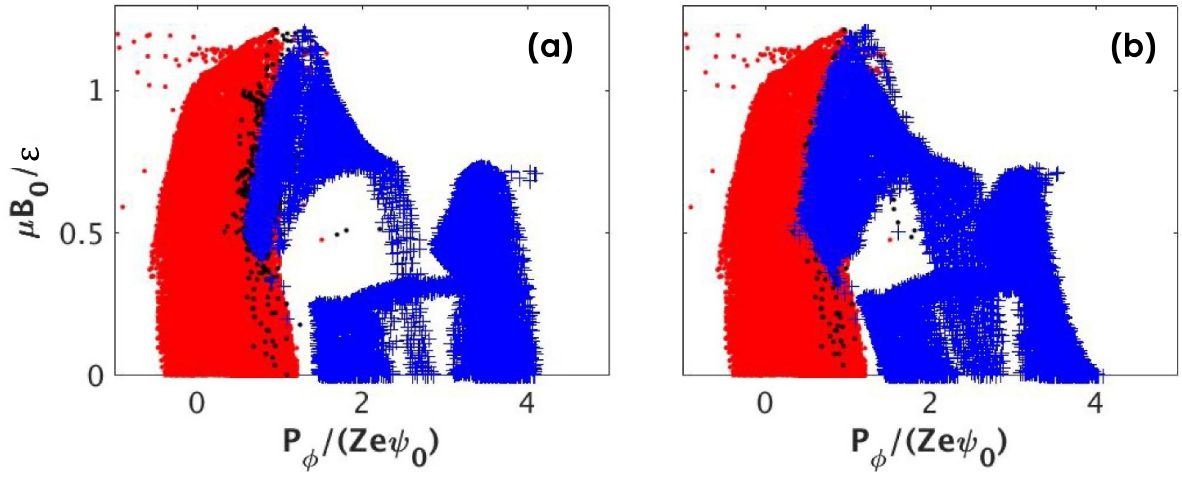

Figure 11. The final locations of all particle markers in the 2D phase space of P_ϕ and $\mu B_0/\varepsilon$, with the maximum tracing time of $30\,000\tau_A$ (23.8 ms). All markers are launched from inside the plasma according to the equilibrium distribution, and classified in three groups according to the final location: those confined inside the plasma (red dots), those confined in the vacuum region outside the plasma after the maximum tracing time (black dots) and those lost to the limiting surface (blue '+'). Plotted here are results from two simulations following (a) the FI guiding-center all the way to the limiting surface, and (b) the FI guiding-center inside the plasma but taking into account the full orbit (i.e. finite gyro-radius) effect as the particle approaches the limiting surface. The overall magnitude of the $n = 1$ TM+IK perturbation inside the plasma is assumed to be 100 G (for the peak value of the normal magnetic field component).

equilibrium, inclusion of higher-order Larmor radius corrections was found to reduce the predicted EP losses (more precisely the resulting heat flux) by about 6% compared to the lowest-order guiding-center result [24]. As for the next justification, most of EPs simulated here have the energy level well below 50 keV as shown in figure 9(a).

Note that like figures 7(a), 10 shows three groups of FIs—those confined inside the plasma, confined outside the plasma, and those lost to the limiting surface. The "wetted" areas on the limiting surface are generally also similar to those in figure 7(a) as mentioned earlier. Comparing figures 10(a) and (b), we note two important differences in the particle loss patterns: (i) a fraction of FIs strike the limiting surface before the particle guiding-centers reach the surface. This is a pure finite gyro-radius effect. (ii) The same effect also prevents particles from entering deep into the upper-right corner of the divertor chamber.

Figure 11 shows the final locations of the same FIs (as from figure 10) in the 2D phase space of $(P_\phi, \mu B_0/\varepsilon)$. It is evident that (i) both passing and trapped particles can strike the limiting surface, and (ii) lost ions (in blue) do not uniformly fill the 2D phase space. On the other hand, the holes/gaps in the 2D "loss"-space are reduced by the full-orbit effect. We also note the similar shape of the confined particle regions (in red) from figure 11 to that of the initial distribution shown in figure 9(b), especially from the left-hand side with more negative values of P_ϕ. This indicates that most of the lost FIs are those launched near the plasma edge (corresponding to larger P_ϕ-values).

Lastly, we report the REORBIT-simulated time traces of the particle loss fraction, evaluated for both the 'GC'- and 'FO'-approaches (figure 12). Here, the loss fraction is defined as the 'weighted' number of lost particles as a proportion of the total. In other words, a weighting factor, proportional to the initial equilibrium distribution function (see figure 9(a)), is assigned to each particle marker when calculating the loss fraction. For the modeled MAST-U discharge 46 493, we find that slightly over 10% of the FIs are lost due to the $n = 1$ TM-IK instability. The loss fraction is higher with the 'FO'-approach as expected, but not by a significant amount.

The EP tracing results reported so far ignored the electric field effect. Inclusion of the electric field (both the equilibrium and the perturbed parts) reduces the particle loss rate as shown in figure 12(the black curve). Here, both the equilibrium and the perturbed electric fields are associated with the $\mathbf{V} \times \mathbf{B}$ term as well as the $\eta\mathbf{J}$ term. The large role is played by the equilibrium electric field associated with toroidal flow of the plasma (see figure 2(d)). Note that this flow profile (and consequently the electric field) lacks a pedestal structure due to measurement limitations. A shaped electric field near the plasma edge may also affect EP losses, which is not studied here. With the above assumptions, the electric field appears to lead to better confinement of certain portion of particles and delay the time for their eventual losses. These are largely particles with super-banana orbits which are located not too close to the plasma edge. Finally, we note the loss fraction saturates within the assumed time interval of the particle tracing.

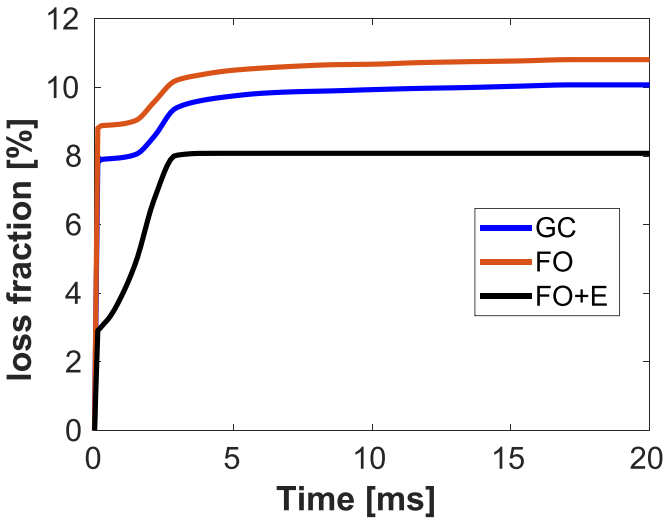

Figure 12. Simulated FI loss fraction versus particle tracing time in the presence of an $n = 1$ TM+IK perturbation with peak value of the normal magnetic field component assumed to be 100 G inside the plasma. All markers are launched from inside the plasma according to the equilibrium distribution. Shown here are results from three simulations following (a) the FI guiding-center ('GC') all the way to the limiting surface, (b) the FI guiding-center inside the plasma but taking into account the full orbit ('FO', i.e. the finite gyro-radius) effect as the particle approaches the limiting surface, and (c) similar to (b) but with inclusion of the electric field effect. Vanishing electric field is assumed in (a) and (b).

5. Conclusion

We have modeled FI losses due to TM-IK instabilities in MAST-U discharges, utilizing the MARS-F MHD stability code and the REORBIT test particle guiding-center orbit-following module. We have focused on MAST-U discharge 46 943 where continuous $n = 1$ TM activity was clearly observed, while also considering discharge 45 163 for a complementary investigation. Indeed, with the experimental plasma toroidal rotation and including the effects of anisotropic thermal transport, MARS-F reveals an $n = 1$ unstable mode in discharge 46 943, which possesses both IK and tearing components. For discharge 45 163, only the IK instability is found using MARS-F. FI loss studies were then carried out using the MARS-F computed eigenmode to represent the 3D field perturbation structure, while assuming certain values for the overall perturbation amplitude.

With a peak perturbation of 100 G inside the plasma (corresponding to ∼6 G at the Mirnov probe location at the outboard mid-plane), REORBIT shows about 10% of the FIs being lost for discharge 46 943, the majority of these (around 90%) being prompt losses and the remainder caused by the presence of the TM-IK. We point out that this result is likely conservative (in terms of the FI confinement) since a 100 G magnetic perturbation is already large compared to the equilibrium poloidal field in MAST-U. Taking into account the finite gyro-orbit effect, as the particle approaches the limiting surface (where particles are lost), only slightly increases the predicted final loss fraction. Inclusion of the electric field during the particle tracing on the other hand reduces the loss rate. Losses occur for both passing and trapped ions. We emphasize that these results were obtained by following ∼100 000 particle markers sampled from the ASCOT-simulated 4D equilibrium distribution of FIs. Detailed particle tracing, assuming a uniform initial distribution in the 2D phase spaces (at given radial locations), reveals that initially counter-current FIs launched near the plasma edge are subject to significant (prompt) losses, with almost all initially co-current ions remaining well confined at the assumed perturbation level.

Most lost FIs strike the lower-half of the limiting surface (as expected, given that the ion ∇B drift direction is down), with a few striking the upper-half regions. As an interesting observation, we find that finite gyro-radius effects prevent lost particles from striking the top-outer corner of the divertor chamber. We also find that a small fraction of FIs remain confined in the vacuum region just outside the plasma without striking the limiting surface, even after a rather long tracing time (> 20 ms).

Assuming the same overall perturbation level inside the plasma, the IK perturbation only (discharge 45 163) is found to produce larger FI losses than the TM-IK compound (discharge 46 943), especially for counter-current ions. A scan of the perturbation level (based on discharge 45 163) finds, not surprisingly, approximately linear scaling of the particle loss fraction (for counter-current FIs) with respect to the perturbation amplitude.

We emphasize that the present study only considers FI losses due to 3D perturbations associated with MHD events. Other (non-3D) effects may also play important roles. In particular, change-exchange with edge neutrals has been found to cause significant beam-ion losses in MAST-U [25, 26].

We also emphasize that this work only presents the first attempt to quantify the MHD-induced EP orbit losses in MAST-U. In view of the significant importance of this issue

(and potentially severe consequences for ST devices), further studies are certainly needed both on the modeling side and from the experimental side (e.g. further calibration of the EP diagnostics). On the modeling side, we foresee several aspects that can be improved in the future modeling: (i) inclusion of higher-order Larmor radius corrections to the present guiding-center model or fully 6D orbit tracing; (ii) consider toroidal asymmetry of the initial distribution of EPs (associated with the NBI beam box location) instead of the relaxed distribution as adopted in this study, and understand the role of the relative phase of the MHD perturbation with respect to the asymmetric toroidal distribution in EPs losses. These aspects are better addressed by the ASCOT code. A code coupling interface between MARS-F and ASCOT is being developed for this purpose. The EP loss rate reported in the present work likely provides a conservative (upper) limit, since taking into account higher-order corrections appear to further reduce orbit losses [24].

Data availability statement

The data cannot be made publicly available upon publication because we do not want the misuse of the data. The data that support the findings of this study are available upon reasonable request from the authors.

Acknowledgments

This material is based upon work supported by the U.S. Department of Energy, Office of Science, Office of Fusion Energy Sciences, under Awards DE-SC0018992 and DE-FG02-95ER54309. This work has also been carried out within the framework of the EUROfusion Consortium, funded by the European Union via the Euratom Research and Training Programme (Grant Agreement No 101052200 – EUROfusion) and from the EPSRC [Grant number EP/W006839/1].

Disclaimer

Appendix. Adding finite gyro-radius to particle guiding-center motion in curvilinear coordinates

Since the REORBIT module has been implemented in curvilinear coordinates $\mathbf{r} \equiv (s, \chi, \phi)$ based on the equilibrium magnetic flux-surface and adopted by the MHD stability analysis in MARS-F, we also implemented an ad hoc addition of the gyro-motion to the guiding-center motion in the same coordinates. Specifically, we follow

$$\mathbf{r}_{\rm FO} - \mathbf{r}_{\rm GC} = d\mathbf{r} = \mathbf{e}_s ds + \mathbf{e}_\chi\, d\chi + \mathbf{e}_\phi\, d\phi = \rho \mathbf{u}, \tag{12}$$

where s labels the flux surface, χ the generalized poloidal angle and ϕ the geometric toroidal angle. $(\mathbf{e}_s, \mathbf{e}_\chi, \mathbf{e}_\phi)$ denote the covariant basis vectors. ρ is the particle Larmor radius evaluated at the given guiding-center location $\mathbf{r}_{\rm GC}$, and $\mathbf{u} = u_1 \nabla s + u_2 \nabla\chi + u_3 \nabla\phi$ is a unit vector (to be identified) perpendicular to the guiding-center velocity $\mathbf{v}_{\rm GC} = \mathbf{v}_{||} + \mathbf{v}_d$ (see equation (10)). Specifically, we have

$$(\mathbf{u} \cdot \mathbf{v}_{\rm GC}) = 0 \quad \text{and} \quad ||\mathbf{u}|| = 1, \tag{13}$$

where $\mathbf{v}_{\rm GC} = v^1 \mathbf{e}_s + v^2 \mathbf{e}_\chi + v^3 \mathbf{e}_\phi$ is a known quantity during guiding-center tracing of the particle. The above two conditions suffice for obtaining

$$u_1 = \cos\alpha / \sqrt{A}, \tag{14}$$

$$u_2 = \sin\alpha / \sqrt{A}, \tag{15}$$

$$u_3 = -\frac{v^1}{v^3} u_1 - \frac{v^2}{v^3} u_2, \tag{16}$$

where $\alpha \in [0, 2\pi]$ is the gyro-angle and

$$A = \left[g^{ss} + \left(\frac{v^1}{v^3}\right)^2 g^{\phi\phi} \right] \cos^2\alpha + 2 \left[g^{s\chi} + \frac{v^1}{v^3}\frac{v^2}{v^3} g^{\phi\phi} \right] \cos\alpha \sin\alpha + \left[g^{\chi\chi} + \left(\frac{v^2}{v^3}\right)^2 g^{\phi\phi} \right] \sin^2\alpha. \tag{17}$$

The metric coefficients g^{ij} from the above equation are also evaluated at the guiding-center location $\mathbf{r}_{\rm GC}$. Knowing the $\mathbf{u}$-vector, equation (12) thus gives the (approximate) full orbit location $\mathbf{r}_{\rm FO}$ of the particle.

ORCID iDs

Yueqiang Liu https://orcid.org/0000-0002-8192-8411
J F Rivero-Rodríguez https://orcid.org/0000-0001-5074-0267
J R Harrison https://orcid.org/0000-0003-2906-5097
K G McClements https://orcid.org/0000-0002-5162-509X

References

[1] Fasoli A *et al* 2007 *Nucl. Fusion* **47** S264
[2] McClements K G *et al* 1999 *Plasma Phys. Control. Fusion* **41** 661
[3] Sharapov S E *et al* 2001 *Phys. Lett.* A **289** 127
[4] Heidbrink W W 2008 *Phys. Plasmas* **15** 055501

[5] Varje J *et al* 2016 *Nucl. Fusion* **56** 046014
[6] Sarkimaki K *et al* 2018 *Nucl. Fusion* **58** 076021
[7] Sanchis L *et al* 2021 *Nucl. Fusion* **61** 046006
[8] Chapman I T *et al* 2010 *Nucl. Fusion* **50** 045007
[9] Harrison J R *et al* 2024 *Nucl. Fusion* **64** 112017
[10] Liu Y Q *et al* 2000 *Phys. Plasmas* **7** 3681
[11] Bai X *et al* 2017 *Phys. Plasmas* **24** 102505
[12] Bai X *et al* 2021 *Nucl. Fusion* **61** 066016
[13] Sun X *et al* 2024 *Phys. Plasmas* **31** 013902
[14] Liu Y Q *et al* 2021 *Nucl. Fusion* **61** 116021
[15] Liu Y Q *et al* 2019 *Nucl. Fusiosn* **59** 126021
[16] Liu Y Q *et al* 2021 *Nucl. Fusion* **61** 106029
[17] Pfefferlé D *et al* 2014 *Nucl. Fusion* **54** 064020
[18] Rivero-Rodríguez J F 2024 *Nucl. Fusion* **64** 086025
[19] Rivero-Rodríguez J F 2018 *Rev. Sci. Instrum.* **89** 10I112
[20] Bai X *et al* 2018 *Phys. Plasmas* **25** 090701
[21] Connor J W *et al* 2015 *Plasma Phys. Control. Fusion* **57** 065001
[22] Brunetti D *et al* 2015 *Plasma Phys. Control. Fusion* **57** 054002
[23] Hirvijoki E *et al* 2014 *Comp. Phys. Comm.* **185** 1310
[24] Lanthaler S *et al* 2017 *Plasma Phys. Control. Fusion* **59** 044014
[25] McClements K G *et al* 2018 *Plasma Phys. Control. Fusion* **60** 095005
[26] Ollus P *et al* 2024 *Plasma Phys. Control. Fusion* **66** 025009